J|A|C|S
ARTICLES
Published on Web 03/27/2007

Multinuclear Solid-State NMR Spectroscopy of Doped Lanthanum Fluoride Nanoparticles

Andy Y. H. Lo,[†] Vasanthakumaran Sudarsan,[‡] Sri Sivakumar,[‡] Frank van Veggel,*[,‡] and Robert W. Schurko*[,†]

Contribution from the Department of Chemistry and Biochemistry, University of Windsor, Windsor, Ontario, Canada N9B 3P4, and Department of Chemistry, University of Victoria, Victoria, British Columbia, Canada V8W 3V6

Received November 30, 2006; E-mail: fvv@uvic.ca; rschurko@uwindsor.ca

Abstract: Multinuclear solid-state NMR spectroscopy and powder X-ray diffraction (XRD) experiments are applied to comprehensively characterize a series of pure and lanthanide-doped LaF_3 nanoparticles (NPs) that are capped with di-*n*-octadectyldithiophosphate ligands (Ln^{3+} = diamagnetic Y^{3+} and Sc^{3+} and paramagnetic Yb^{3+} ions), as well as correlated bulk microcrystalline materials (LaF_3, YF_3, and ScF_3). Solid-state ^{139}La and ^{19}F NMR spectroscopy of bulk LaF_3 and the LaF_3 NPs reveal that the inorganic core of the NP retains the LaF_3 structure at the molecular level; however, inhomogeneous broadening of the NMR powder patterns arises from distributions of ^{139}La and ^{19}F NMR interactions, confirming a gradual change in the La and F site environments from the NP core to the surface. ^{139}La and ^{19}F NMR experiments also indicate that low levels (5 and 10 mol %) of Ln^{3+} doping do not significantly change the LaF_3 structure in the NP core. Similar doping levels of paramagnetic Yb^{3+} ions severely broaden ^{19}F resonances, but only marginally effect ^{139}La powder patterns, suggesting that the dopant ions are uniformly distributed throughout the NP core and occupy vacant La sites. Measurements of ^{139}La T_1 and T_2 relaxation constants are seen to vary between the bulk material and NPs and between samples with diamagnetic and paramagnetic dopants. ^{45}Sc NMR experiments confirm that the dopants are integrated into the La sites of the LaF_3 core. Solid-state ^1H and ^{31}P magic-angle spinning (MAS) NMR spectra aid in probing the nature of the capping ligands and their interactions at the NP surface. ^{31}P cross-polarization (CP)/MAS NMR experiments identify not only the dithiophosphate head groups but also thiophosphate and phosphate species which may form during NP synthesis. Finally, $^{19}F-^{31}P$ CP/MAS and ^1H MAS experiments confirm that ligands are coordinated to the NP surface.

Introduction

Lanthanide(III)-doped nanoparticles (NPs) with inorganic cores and outer organic stabilizing ligands are of great interest due to their unique luminescent properties which have made them important in the manufacture of light-emitting diodes (LEDs),[1] liquid−crystal displays,[2] biological assays,[3] nanometer-scale optoelectronic devices,[4] and light sources in zero-threshold lasers.[5] NPs doped with different Ln^{3+} ions produce spectral emissions across visible light (Eu^{3+} and Tb^{3+}) and near-infrared (NIR; Pr^{3+}, Nd^{3+}, Er^{3+}, and Yb^{3+}) regions. NIR-emitting NPs are of particular interest because they are the luminescent elements in polymer-based telecommunication components, lasers, displays, and polymer LEDs. Luminescence in Ln^{3+} ions arises from radiative relaxation after the parity-forbidden transitions within the partially filled 4*f* orbitals that are shielded by the filled 5*s* and 5*p* orbitals. Consequently, *f*−*f* transitions lead to low molar absorption coefficients and slow emission rates, resulting in long luminescent lifetimes.[6]

Polymeric materials are advantageous in the fabrication of optical components because they are easy to process by spin−coating and photolithography.[7] However, direct doping of the Ln^{3+} ions into polymeric materials is not practical because the largely spaced vibrational and/or electronic transitions present in polymers can often quench *f*−*f* transitions associated with the luminescent process. Initially, organic complexes as luminescent materials were studied, but lifetimes of NIR emitters are very short with low (<1%) quantum yields. A more promising strategy is to dope the luminescent Ln^{3+} ion into an inorganic matrix (low phonon matrices) and coat the surface with ligands to fine-tune the processability through dispersion in organic solvents, since the latter have long luminescence

[†] University of Windsor.
[‡] University of Victoria.

(1) Dabbousi, B. O.; Bawendi, M. G.; Onitsuka, O.; Rubner, M. F. *Appl. Phys. Lett.* **1995**, *66*, 1316.
(2) Justel, T.; Nikol, H.; Ronda, C. *Angew. Chem., Int. Ed.* **1998**, *37*, 3085.
(3) Dahan, M.; Laurence, T.; Pinaud, F.; Chemla, D. S.; Alivisatos, A. P.; Sauer, M.; Weiss, S. *Opt. Lett.* **2001**, *26*, 825.
(4) Gonsalves, K. E.; Carlson, G.; Rangarajan, S. P.; Benaissa, M.; JoseYacaman, M. *J. Mater. Chem.* **1996**, *6*, 1451.
(5) Klimov, V. I.; Mikhailovsky, A. A.; Xu, S.; Malko, A.; Hollingsworth, J. A.; Leatherdale, C. A.; Eisler, H. J.; Bawendi, M. G. *Science* **2000**, *290*, 314.
(6) Maas, H.; Currao, A.; Calzaferri, G. *Angew. Chem., Int. Ed.* **2002**, *41*, 2495.
(7) Slooff, L. H.; van Blaaderen, A.; Polman, A.; Hebbink, G. A.; Klink, S. I.; van Veggel, F.; Reinhoudt, D. N.; Hofstraat, J. W. *J. Appl. Phys.* **2002**, *91*, 3955.

Chart 1. Schematic Picture of a Ln^{3+}-Doped LaF_3 Nanoparticle Stabilized by Di-*n*-octadectyldithiophosphate ($^{-}S_2P(OC_{18}H_{37})_2$) Ligands (Ln = Yb, Y, and Sc)

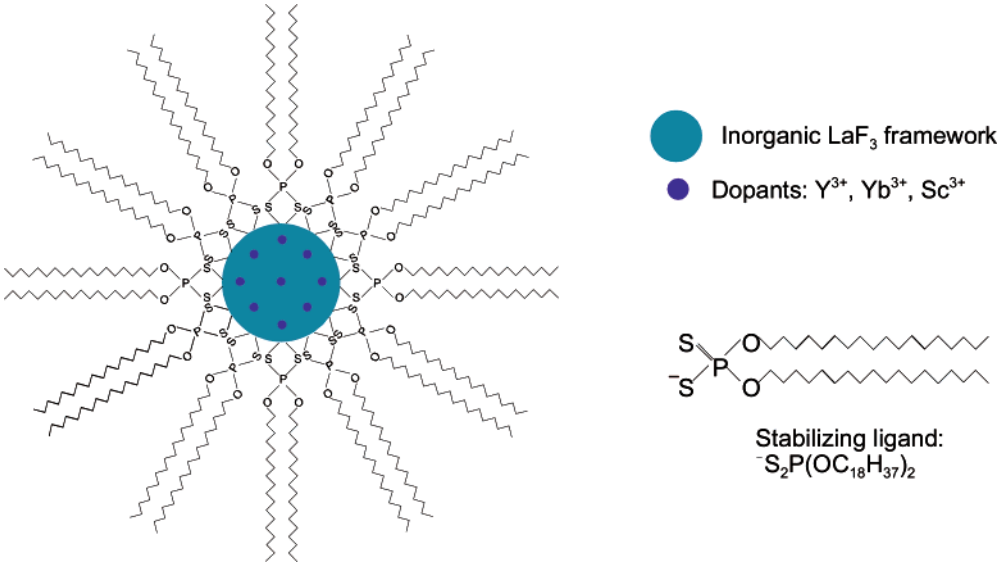

lifetimes and high quantum efficiencies.[8−11] Thus, small amounts of the Ln^{3+} ions are doped into an inorganic framework to minimize the quenching process. In a recent publication, van Veggel et al. have shown that polymer-based optical amplifiers operating at 1.33 μm are possible based on Nd^{3+}-doped LaF_3 NPs.[12] A number of suitable inorganic frameworks such as $LaPO_4$,[13−15] LaF_3,[16,17] Y_2O_3,[18] YBO_3,[19] YVO_4,[20] etc. can be found in the literature. LaF_3 is of interest because it has low vibrational energies; hence, quenching of the luminescence from excited states of Ln^{3+} ions is minimized. A procedure for synthesizing LaF_3 NPs was originally reported by Dang et al.[21] and then modified and optimized to yield luminescent Ln^{3+}-doped NPs.[16]

In order to incorporate the Ln^{3+}-doped inorganic NPs into the organic polymer matrix, it is necessary to increase their solubility. This is accomplished by coating the NPs with surfactants or so-called "stabilizing ligands". These ligands are typically composed of a polar inorganic "head" which coordinates to the NP surface and a nonpolar alkyl hydrocarbon "tail". In particular, ammonium di-*n*-octadectyldithiophosphate, $[NH_4][S_2P(OC_{18}H_{37})_2]$, was originally used to stabilize the Ln^{3+}-doped LaF_3 NPs in the organic matrix; however, other ligands have also been synthesized and attached to the NPs to improve solubility for different organic environments.[22] The ligands are used to (i) prevent aggregation of NPs, (ii) control the growth/size of the particles, and (iii) ensure the NPs are homogeneously distributed within the polymer matrix.

Ln^{3+}-doped LaF_3 NPs have been characterized by a number of techniques. Transmission electron microscopy (TEM) and powder X-ray diffraction (XRD) were used to determine the size and crystallinity, respectively, of the NPs. X-ray fluorescence (XRF) and elemental analysis are also routinely applied for analysis of composition. Emission/excitation and luminescence spectroscopies have been utilized to observe luminescent properties of particles with different Ln dopants.[16,17,22,23] Solution ^{1}H NMR spectroscopy has been applied for characterization of the di-*n*-octadectyldithiophosphate stabilizing ligand of the LaF_3 NPs.[17,22,23] To the best of our knowledge, there have not been any solid-state NMR experiments performed on this class of NPs. To date, statements about the molecular structure have been made only by inference, and no direct information on the ligand−NP surface interactions has been obtained.[16,17,22] Solid-state NMR spectroscopy is the ideal technique for characterization of such structural features.

In this work, we present a comprehensive multinuclear solid-state NMR characterization of pure and doped (Yb^{3+}, Y^{3+}, and Sc^{3+}) LaF_3 NPs which are coordinated with di-*n*-octadectyldithiophosphate stabilizing ligands (Chart 1). To examine the structural order and crystallinity of the inorganic cores of the NPs, as well as the effects of doping with rare earth and lanthanide ions, solid-state ^{139}La and ^{19}F NMR experiments were conducted on bulk crystalline LaF_3, pristine LaF_3 NPs, and doped LaF_3 NPs. Solid-state ^{89}Y and ^{45}Sc NMR experiments were used to attempt identification of yttrium/scandium sites upon doping with Y^{3+}/Sc^{3+}. Solid-state ^{1}H and ^{31}P NMR

(8) Hebbink, G. A.; Reinhoudt, D. N.; van Veggel, F. *Eur. J. Org. Chem.* **2001**, 4101.
(9) Klink, S. I.; Hebbink, G. A.; Grave, L.; Peters, F. G. A.; van Veggel, F.; Reinhoudt, D. N.; Hofstraat, J. W. *Eur. J. Org. Chem.* **2000**, 1923.
(10) Wolbers, M. P.O.; van Veggel, F. C. J. M.; SnellinkRuel, B. H. M.; Hofstraat, J. W.; Geurts, F. A. J.; Reinhoudt, D. N. *J. Am. Chem. Soc.* **1997**, *119*, 138.
(11) Slooff, L. H.; Polman, A.; Klink, S. I.; Hebbink, G. A.; Grave, L.; van Veggel, F.; Reinhoudt, D. N.; Hofstraat, J. W. *Opt. Mater.* **2000**, *14*, 101.
(12) Dekker, R.; Klunder, D. J. W.; Borreman, A.; Diemeer, M. B. J.; Worhoff, K.; Driessen, A.; Stouwdam, J. W.; van Veggel, F. C. J. M. *Appl. Phys. Lett.* **2004**, *85*, 6104.
(13) Hebbink, G. A.; Stouwdam, J. W.; Reinhoudt, D. N.; Van Veggel, F. C. J. M. *Adv. Mater.* **2002**, *14*, 1147.
(14) Riwotzki, K.; Meyssamy, H.; Kornowski, A.; Haase, M. *J. Phys. Chem. B* **2000**, *104*, 2824.
(15) Riwotzki, K.; Meyssamy, H.; Schnablegger, H.; Kornowski, A.; Haase, M. *Angew. Chem., Int. Ed.* **2001**, *40*, 573.
(16) Stouwdam, J. W.; van Veggel, F. C.J. M. *Nano Lett.* **2002**, *2*, 733.
(17) Stouwdam, J. W.; Hebbink, G. A.; Huskens, J.; van Veggel, F. C. J. M. *Chem. Mater.* **2003**, *15*, 4604.
(18) Zhang, W.-W.; Xu, M.; Zhang, W.-P.; Yin, M.; Qi, Z.-M.; Xia, S. D.; Garapon, C. *Chem. Phys. Lett.* **2003**, *376*, 318.
(19) Jiang, X.-C.; Yan, C.-H.; Sun, L.-D.; Wei, Z.-G.; Liao, C.-S. *J. Solid State Chem.* **2003**, *175*, 245.
(20) Yan, C.-H.; Sun, L.-D.; Liao, C.-S.; Zhang, Y.-X.; Lu, Y.-Q.; Huang, S.-H.; Lu, S.-Z. *Appl. Phys. Lett.* **2003**, *82*, 3511.
(21) Zhou, J. F.; Wu, Z. S.; Zhang, Z. J.; Liu, W. M.; Dang, H. X. *Wear* **2001**, *249*, 333.
(22) Stouwdam, J. W.; van Veggel, F. C. J. M. *Langmuir* **2004**, *20*, 11763.
(23) Sudarsan, V.; van Veggel, F. C. J. M.; Herring, R. A.; Raudsepp, M. *J. Mater. Chem.* **2005**, *15*, 1332.

experiments were carried out on selected samples to examine the nature of the stabilizing ligands and their interactions with the inorganic cores. Solid-state NMR spectroscopy is applied to investigate a number of facets of NP core and surface structure, as well as their interface, including the following: (i) the degree of disorder in the NP core, (ii) existence of Ln doping either in interstitial sites of the LaF_3 matrix or at crystallographic lanthanum sites, (iii) structural changes in the inorganic core resulting from doping, (iv) chemical changes in the stabilizing ligands over time, and (v) nature of the interactions between the stabilizing ligands and inorganic cores.

Experimental Section

Sample Preparation and Handling. Crystalline, anhydrous LaF_3, YF_3, and ScF_3 were purchased from Strem and used without further purification, with the exception of YF_3 which was dried under a vacuum at ca. 120 °C for over 8 h. Pure LaF_3 NPs and those doped with Yb^{3+}, Y^{3+}, and Sc^{3+} were synthesized according to literature procedures.[16,17] All samples were packed into zirconia rotors for NMR experiments.

Solid-State NMR. Most solid-state NMR experiments were conducted on a Varian Infinity Plus NMR spectrometer with a 9.4 T wide-bore Oxford magnet, operating at $\nu_0(^{139}La) = 56.46$ MHz, $\nu_0(^{45}Sc) = 97.10$ MHz, $\nu_0(^{19}F) = 376.06$ MHz, $\nu_0(^{89}Y) = 19.59$ MHz, $\nu_0(^{1}H) = 399.73$ MHz, and $\nu_0(^{31}P) = 161.81$ MHz. Typical ^{1}H and ^{19}F decoupling with rf fields ranging from 60 to 123 kHz were applied where appropriate. Varian/Chemagnetics 2.5 mm HX, 4 mm HX, and 5 mm HXY magic-angle spinning (MAS) probes were utilized for all experiments. Tuning and matching for low-frequency (i.e., 19.59 MHz) experiments were accomplished with a Varian/Chemagnetics low-gamma tuning box. Hahn-echo pulse sequences of the form $[(\pi/2)_x-\tau_1-(\pi)_y-\tau_2-\text{acquire}]$ (where τ_1 and τ_2 are the interpulse delays) were applied in most of the solid-state NMR experiments, since standard Bloch-decay acquisitions of broad NMR spectra resulted in the loss of points at the beginning of the FID, giving rise to spectral artifacts and baseline distortions. Additional solid-state ^{45}Sc MAS NMR experiments were conducted on a 900 MHz Bruker AVANCE-II NMR spectrometer, operating at $\nu_0(^{45}Sc) = 218.68$ MHz. Further details concerning experimental parameters can be found in the Supporting Information (Tables S1 to S7).

Lanthanum chemical shifts were referenced to a 1.0 M aqueous $LaCl_3$ solution ($\delta_{iso}(^{139}La) = 0.0$ ppm). The central−transition (CT) selective $\pi/2$ pulse widths (i.e., real $\pi/2$ pulse scaled by $(I + {}^1/_2)^{-1}$) ranged from 0.76 μs to 1.1 μs (rf fields ranged from 60 to 80 kHz). For rotor-synchronized MAS NMR experiments, a Rotor−Assisted Population Transfer (RAPT) pulse scheme[24] was applied prior to the Hahn-echo sequence for signal enhancement. For both MAS and static NMR experiments, calibrated recycle delays were 1.0 s or less, and between 30 000 and 330 000 transients were acquired.

Fluorine chemical shifts were referenced to neat $CFCl_3$ liquid ($\delta_{iso}(^{19}F) = 0.0$ ppm). For all MAS experiments, $\pi/2$ pulse widths were ca. 2.0 μs. Calibrated recycle delays ranged from 8 to 300 s, and between 384 and 7624 transients were collected. Proton chemical shifts were referenced to TMS ($\delta_{iso}(^1H) = 0.0$ ppm) by using solid adamantane as a secondary reference, setting the ^{1}H NMR resonance to 1.85 ppm. $\pi/2$ pulse widths between 2.0 μs and 4.1 μs were applied to all ^{1}H Bloch-decay MAS NMR experiments. Recycle delays were from 1 to 4 s, and four transients were collected for each experiment. Phosphorus chemical shifts were referenced to an 85% H_3PO_4 solution ($\delta_{iso}(^{31}P) = 0.0$ ppm). Solid-state $^{31}P\{^1H\}$ MAS NMR experiments involved $\pi/2$ pulse widths of 4.7 μs ($\nu_1(^{31}P) = 25$ kHz), calibrated recycle delays between 5 and 40 s, and the acquisition of 528 to 4288 transients. ^{1}H−^{31}P and ^{19}F−^{31}P variable-amplitude cross-polarization MAS (VACP/MAS) NMR experiments involved rf powers of 90 to 123 kHz in the Hartmann−Hahn match for both ^{1}H/^{19}F and ^{31}P channels. Contact times varied from 2 to 12 ms, and the longest recycle delay of 60 s was utilized. Yttrium chemical shifts were referenced to a 1.0 M YCl_3 aqueous solution ($\delta_{iso}(^{89}Y) = 0.0$ ppm) by setting the NMR resonance in solid $Y(NO_3)_3{\cdot}6H_2O$ (as a secondary reference) to −53.0 ppm.[25] Bloch-decay $^{89}Y\{^{19}F\}$ MAS NMR experiments involved a $\pi/2$ pulse of 20.0 μs ($\nu_1(^{89}Y) = 11.1$ kHz), a 300 s recycle delay, and an acquisition of 500 scans. ^{19}F−^{89}Y VACP/MAS NMR experiments utilized a pulse width of 2.8 μs, a Hartmann−Hahn matching rf field of 13 to 18 kHz, 30 to 60 s calibrated recycle delays, 30 to 40 ms contact times and involved the collection of 880 to 1452 transients. Scandium chemical shifts were referenced to a 0.11 M $ScCl_3$ solution in 0.05 M HCl ($\delta_{iso}(^{45}Sc) = 0.0$ ppm).[26,27] In ^{45}Sc MAS NMR experiments, 0.43 μs $\pi/2$ pulses and 5 s recycle delays were utilized, and 9031 scans were collected.

Room-temperature ^{139}La longitudinal (T_1) and transverse (T_2) relaxation measurements were conducted on bulk LaF_3, as well as pure and Yb^{3+}-doped LaF_3 NPs. T_1 constants were determined using saturation recovery.[28] The quadrupolar Carr−Purcell Meiboom−Gill (QCPMG) pulse sequence[29] was applied to stationary samples for the measurement of T_2 time constants. Extraction of T_1 time constants was accomplished from the functions $y(\tau) = A \times [1 - \exp(-\tau/T_1)]$ and $y(\tau) = A_f \times [1 - \exp(-\tau/T_{1f})] + A_s \times [1 - \exp(-\tau/T_{1s})]$ for mono- and biexponential curve fits, respectively, while for T_2 time constants functions such as $y(\tau) = B \times \exp(-\tau/T_2)$ and $y(\tau) = B_f \times \exp(-\tau/T_{2f}) + B_s \times \exp(-\tau/T_{2s})$ were utilized. The subscripts "f" and "s" in the above functions indicate the "fast" and "slow" contributions to relaxation (*vide infra*).

Spectral Simulations. The EFG tensor parameters of ^{139}La static and MAS NMR spectra of bulk LaF_3 were obtained from analytical and numerical simulations using the WSOLIDS[30] and SIMPSON[31] simulation packages, respectively. The latter is installed on a Dell Precision 420 workstation with a dual 3.6 GHz Xenon Precision 670n workstation running Red Hat Linux 9.0. SIMPSON simulations were carried out by the *direct* method with powder averaging using the *zcw4180* crystal file, which is provided with the package. I_{1z} was set as the start detect operator, while I_{1p} or I_{1c} (with and without consideration of satellite transitions (STs), respectively) was set as the detect operator. The number of gamma angles was set to 63 and 18 for $\nu_{rot} = 16$ and 28 kHz, respectively.

Powder X-ray Diffraction. Powder X-ray diffraction (XRD) experiments were conducted on samples loaded into 1.0 mm o.d. capillary tubes using a Bruker AXS D8 DISCOVER powder X-ray diffractometer, which utilizes a Cu Kα_2 ($\lambda = 1.540\,56$ Å) radiation source with a Bruker AXS HI-STAR area detector. Simulations of powder XRD patterns from known crystal structures[32−38] were performed using PowderCell software.[39]

(24) Yao, Z.; Kwak, H. T.; Sakellariou, D.; Emsley, L.; Grandinetti, P. J. *Chem. Phys. Lett.* **2000**, *327*, 85.

(25) Merwin, L. H.; Sebald, A. *J. Magn. Reson.* **1990**, *88*, 167.
(26) Haid, E.; Koehnlein, D.; Koessler, G.; Lutz, O.; Messner, W.; Mohn, K. R.; Nothaft, G.; van Rickelen, B.; Schich, W.; Steinhauser, N. *Z. Naturforsch., A: Phys. Sci.* **1983**, *38A*, 317.
(27) Rossini, A. J.; Schurko, R. W. *J. Am. Chem. Soc.* **2006**, *128*, 10391.
(28) Markley, J. L.; Horsley, W. J.; Klein, M. P. *J. Chem. Phys.* **1971**, *55*, 3604.
(29) Larsen, F. H.; Jakobsen, H. J.; Ellis, P. D.; Nielsen, N. C. *J. Phys. Chem. A* **1997**, *101*, 8597.
(30) Eichele, K.; Wasylishen, R. E. *WSOLIDS*, v. 1.17.30 ed.; Tübingen, Germany, 2001.
(31) Bak, M.; Rasmussen, J. T.; Nielsen, N. C. *J. Magn. Reson.* **2000**, *147*, 296.
(32) Zalkin, A.; Templeton, D. H. *J. Am. Chem. Soc.* **1953**, *75*, 2453.
(33) Cheetham, A. K.; Norman, N. *Acta Chem. Scand.* **1974**, *28*, 55.
(34) Rotereau, K.; Gesland, J. Y.; Daniel, P.; Bulou, A. *Mater. Res. Bull.* **1993**, *28*, 813.
(35) Nowacki, W. *Naturwissenschaften* **1938**, *26*, 801.
(36) Nowacki, W. *Z. Kristallogr. Kristallgeom. Kristallphys. Kristallchem.* **1939**, *101*, 273.
(37) Ippolitov, E. G.; Maklachkov, A. G. *Zhurnal Neorg. Khimii* **1970**, *15*, 1466.
(38) Loesch, R.; Hebecker, C.; Ranft, Z. *Z. Anorg. Allg. Chem.* **1982**, *491*, 199.
(39) Kraus, W.; Nolze, G. *PowderCell*, v. 2.4 ed.; Federal Institute for Materials Research and Testing: Berlin, Germany, 2000.

Chart 2. (A and B) Rotation of a LaF_{11} Unit about the La−F3 Bond (Parallel to *a*-Axis of the Unit Cell) by 180° Illustrating a Local C_2 Symmetry in **1** and (C) Extended Structure of **1**

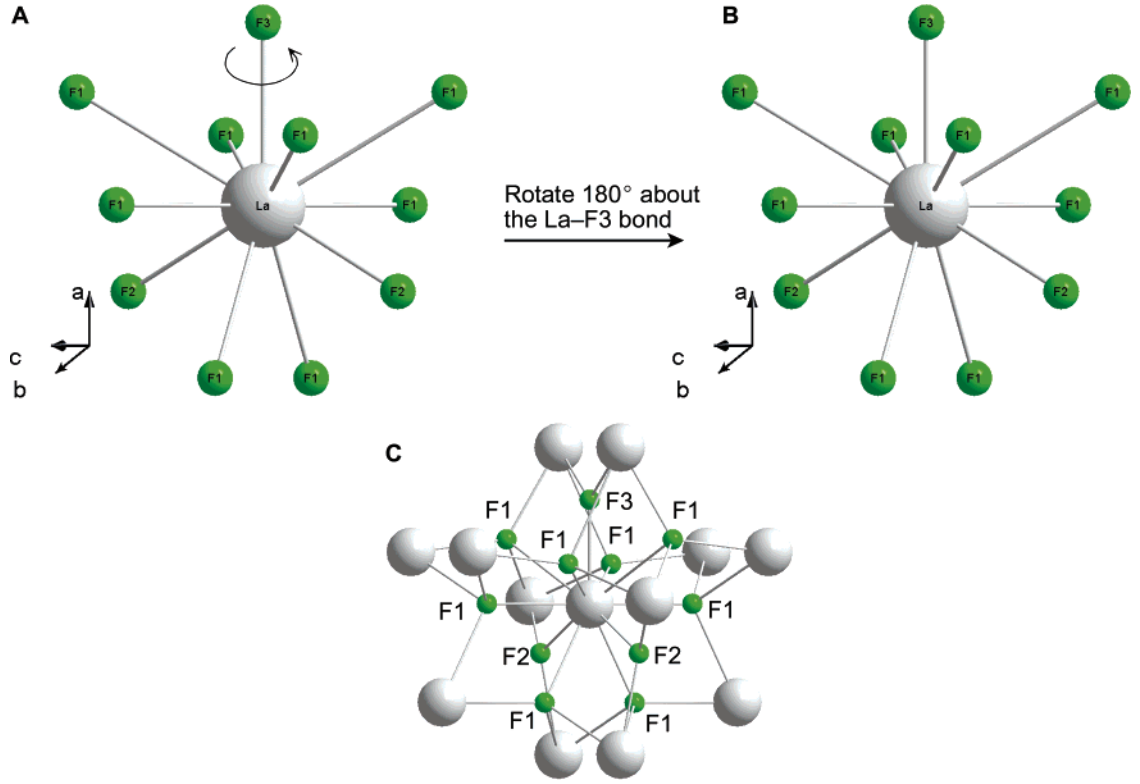

Results and Discussion

This section is organized as follows: NMR characterization of bulk crystalline LaF_3 (**1**) is presented, followed by a comparison with the undoped parent LaF_3 NPs (**2**). The NMR spectra of the LaF_3 NPs doped with 5 and 10 mol % paramagnetic Yb^{3+} ions (**3** and **4**, respectively; dopant concentrations are calculated relative to the number of moles of Ln^{3+}) are compared with those of **2**. ^{139}La spin−lattice (T_1) and spin−spin (T_2) relaxation data for **1**, **2**, and **4** as well as NMR data for LaF_3 NPs doped with diamagnetic Y^{3+} (5 and 10 mol %) and Sc^{3+} (10 mol %) ions (samples **5**, **6**, and **7**, respectively) are discussed. Solid-state ^{89}Y and ^{45}Sc NMR spectra of bulk YF_3 (**8**) and ScF_3 (**9**) are used for comparison with diamagnetically doped samples. Finally, the stabilizing ligands, which are expected to be coordinated to the surface of NPs, are examined by ^{1}H MAS, ^{31}P{^{1}H} MAS, ^{1}H−^{31}P variable-amplitude cross-polarization MAS (VACP/MAS), and ^{19}F−^{31}P VACP/MAS NMR experiments.

Bulk Crystalline Lanthanum Trifluoride, 1. LaF_3 has been well characterized by a number of techniques, including single-crystal X-ray[40−46] and neutron[47] diffraction, solid-state ^{19}F NMR[48−54] and ^{139}La NMR,[54,55] as well as variable-temperature ^{139}La nuclear quadrupole resonance (NQR) experiments.[56,57] Numerous structures of LaF_3 have been reported involving different space groups, cell dimensions, and atomic positions (see above references). The currently accepted structure is found in a combined X-ray and neutron-diffraction study on a single-crystal of LaF_3 by Maximov et al.[46] They reported a single lanthanum site and three distinct fluorine sites (denoted as F1, F2, and F3); however, the fluoride ions are known to undergo dynamic exchange, which may be largely responsible for the ionic conduction in LaF_3.[50−53,58] The local structure centered at the La site is depicted in Chart 2A. The La atom is 11-coordinate and has C_2 symmetry, with eight F1, two F2, and one F3 positions. The rotational axis lies along the lone La−F3 bond which is also parallel to the crystallographic *a*-axis (Chart 2A,B). The ratio of F1/F2/F3 sites in the unit cell is 6:2:1. Each of the F1 atoms is shared between four different La atoms in a tetrahedral arrangement, while each of the F2 and F3 atoms is shared by three La atoms in trigonal pyramidal and trigonal planar coordination environments, respectively (Chart 2C). Our room-temperature ^{19}F MAS NMR spectrum of

(40) Schlyter, K. *Ark. Kemi* **1952**, *5*, 73.
(41) Wyckoff, R. W. G. *Crystal Structures*; Interscience Publishers: New York, 1963; Vol. 2.
(42) Mansmann, M. *Z. Anorg. Allg. Chem.* **1964**, *331*, 98.
(43) Mansmann, M. *Z. Kristallogr. Kristallgeom. Kristallphys. Kristallchem.* **1966**, *122*, 375.
(44) Zalkin, A.; Templeton, D. H.; Hopkins, T. E. *Inorg. Chem.* **1966**, *5*, 1466.
(45) de Rango, C.; Tsoucaris, G.; Zelwer, C. *C. R. Seances Acad. Sci. C* **1966**, *263*, 64.
(46) Maximov, B.; Schulz, H. *Acta Crystallogr., Sect. B* **1985**, *41*, 88.
(47) Gregson, D.; Catlow, C. R. A.; Chadwick, A. V.; Lander, G. H.; Cormack, A. N.; Fender, B. E.F. *Acta Crystallogr., Sect. B* **1983**, *39*, 687.
(48) Saraswati, V.; Vijayaraghavan, R. *Phys. Lett.* **1966**, *21*, 363.
(49) Saraswati, V.; Vijayaraghavan, R. *J. Phys. Chem. Solids* **1967**, *28*, 2111.
(50) Jaroszkiewicz, G. A.; Strange, J. H. *J. Phys. C: Solid State Phys.* **1985**, *18*, 2331.
(51) Aalders, A. F.; Arts, A. F. M.; De Wijn, H. W. *Phys. Rev. B* **1985**, *32*, 5412.
(52) Privalov, A. F.; Cenian, A.; Fujara, F.; Gabriel, H.; Murin, I. V.; Vieth, H. M. *J. Phys.: Condens. Matter* **1997**, *9*, 9275.
(53) Wang, F.; Grey, C. P. *Chem. Mater.* **1997**, *9*, 1068.
(54) Andersson, L. O.; Proctor, W. G. *Z. Kristallogr.* **1968**, *127*, 366.
(55) Ooms, K. J.; Feindel, K. W.; Willans, M. J.; Wasylishen, R. E.; Hanna, J. V.; Pike, K. J.; Smith, M. E. *Solid State Nucl. Magn. Reson.* **2005**, *28*, 125.
(56) Lee, K.; Sher, A.; Andersson, L. O.; Proctor, W. G. *Phys. Rev.* **1966**, *150*, 168.
(57) Nakamura, N.; Chihara, H. *J. Phys. Chem. Solids* **1987**, *48*, 833.
(58) Goldman, M.; Shen, L. *Phys. Rev.* **1966**, *144*, 321.

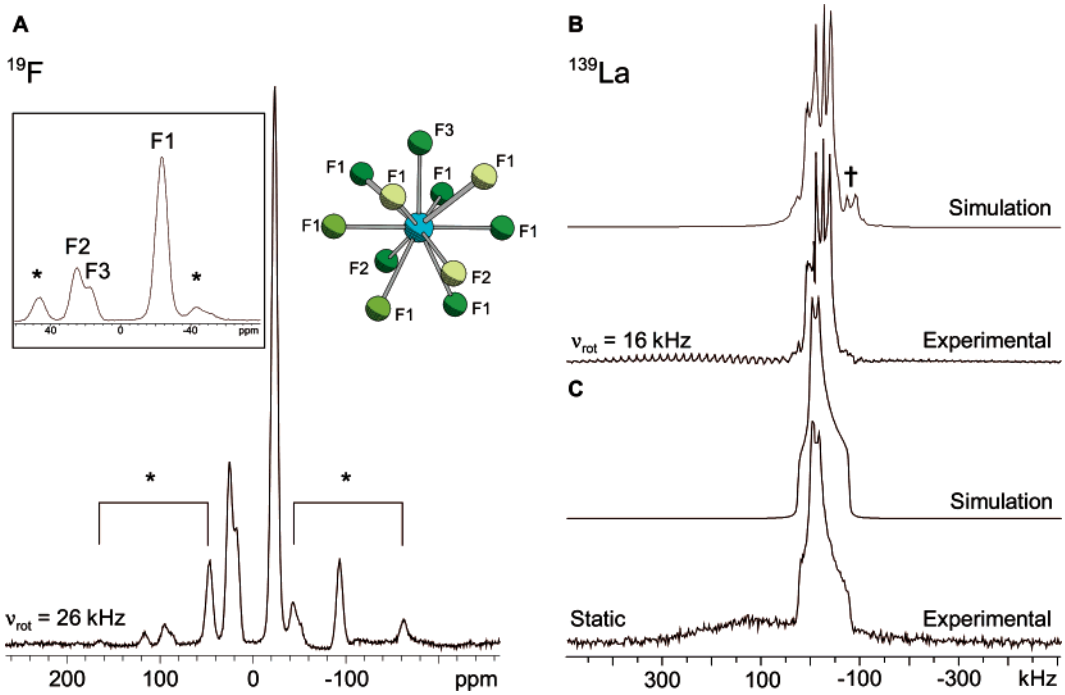

Figure 1. (A) ^{19}F MAS, (B) ^{139}La MAS, and (C) static ^{139}La NMR spectra of **1** acquired at 9.4 T, along with the coordination environment of the La atom in a LaF_{11} unit for reference. Inset of (A): Expansion of the isotropic region, with "*" denoting the spinning sidebands. In (B), the symbol "†" in the numerical simulation indicates a spinning sideband of the central transition and is not observed in the experimental powder pattern due to overlapping satellite transitions (see Figure S2 in the Supporting Information).

crystalline LaF_3 (Figure 1A) shows three distinct ^{19}F resonances centered at −23.5, 24.9, and 17.3 ppm, which are assigned to F1, F2, and F3, respectively (Figure 1A, inset). Deconvolution of the entire NMR powder pattern (i.e., including all spinning sidebands) reveals an F1/F2/F3 ratio of 13.2(2):3.6(4):2.0(4), in good agreement with the previously reported X-ray[46] and NMR[53] data.

^{139}La NMR experiments were also conducted on **1**. Lanthanum has two NMR active isotopes, ^{138}La and ^{139}La, which have spins $I = 5$ and $^7/_2$, respectively. The latter is more favorable for NMR experimentation due to its high natural abundance (99.91%) and smaller nuclear quadrupole moment ($Q(^{139}\text{La}) = 0.20 \times 10^{-28}$ m^2 and $Q(^{138}\text{La}) = 0.45 \times 10^{-28}$ m^2).[59] Solid-state ^{139}La NMR spectroscopy has been applied to study a variety of systems, including LaF_3 single crystals,[54] $La_{1-x}A_xMO_3$ (where A = Sr, Ca and M = Mn, Cr, and Co),[60−63] and $LaMn(O_{1-x}F_x)_3$,[64] as well as for studying cation exchange processes in lanthanum-containing Y zeolites.[65−68] Solid-state ^{139}La NMR experiments have also been conducted on La_2O_3,[69] lanthanum halides (LaX_3 with X = F, Cl, Br, and I),[55] and a variety of complexes,[70,71] to investigate the ^{139}La electric field gradient (EFG) tensors, as well as to test pulse sequences such as quadrupolar phase-adjusted spinning sidebands (QPASS)[72] and fast amplitude modulation (FAM) with a receptive spin-$^7/_2$ nucleus.[73]

The ^{139}La MAS NMR spectrum of **1** is presented in Figure 1B. The complexity of the NMR powder pattern may stem from either (i) overlapping of the central transition (CT) and satellite transitions (STs) or (ii) the presence of multiple lanthanum sites. Comparison of the powder XRD pattern of bulk LaF_3 to a simulated pattern (Figure 2A,B) confirms that there is a single unique La site. In addition, numerical simulation of the MAS NMR pattern utilizing a single La site, with $\delta_{iso} = -130$ ppm, $C_Q = 16.0$ MHz, and $\eta_Q = 0.81$, also confirms this. The ^{139}La static NMR spectrum (Figure 1C) can be simulated with parameters matching that of the ^{139}La MAS NMR data discussed above (the effect of lanthanum chemical shielding anisotropy (CSA) is negligible at 9.4 T; see Figure S1A,B in the Supporting Information). The relatively weak underlying pattern results from partial excitation of the STs (Figure S1C to S1E), since the STs are very intense near the CT for high spin quadrupolar nuclei (e.g., $^7/_2$ or $^9/_2$) with η_Q close to 1. Both MAS and static NMR data provide quadrupolar and chemical shift parameters which are in excellent agreement with previously reported values.[54,55]

(59) Pyykko, P. *Mol. Phys.* **2001**, *99*, 1617.
(60) Savosta, M. M.; Doroshev, V. D.; Kamenev, V. I.; Borodin, V. A.; Tarasenko, T. N.; Mazur, A. S.; Marysko, M. *J. Exp. Theor. Phys.* **2003**, *97*, 573.
(61) Papavassiliou, G.; Fardis, M.; Milia, F.; Pissas, M.; Kallias, G.; Niarchos, D.; Dimitropoulos, C.; Scherrer, P. *Phys. Rev. B* **1998**, *58*, 12237.
(62) Bastow, T. J. *Solid State Nucl. Magn. Reson.* **1994**, *3*, 17.
(63) Hoch, M. J. R.; Kuhns, P. L.; Moulton, W. G.; Reyes, A. P.; Lu, J.; Wu, J.; Leighton, C. *Phys. Rev. B* **2004**, *70*, 174443/1.
(64) Mikhalev, K. N.; Lekomtsev, S. A.; Gerashchenko, A. P.; Yakubovskii, A. Y.; Kaul, A. R. *JETP Lett.* **2003**, *77*, 401.
(65) Hunger, M.; Engelhardt, G.; Weitkamp, J. *Stud. Surf. Sci. Catal.* **1994**, *84*, 725.
(66) Engelhardt, G.; Hunger, M.; Koller, H.; Weitkamp, J. *Stud. Surf. Sci. Catal.* **1994**, *84*, 421.
(67) Hunger, M.; Engelhardt, G.; Weitkamp, J. *Microporous Mater.* **1995**, *3*, 497.
(68) Herreros, B.; Man, P. P.; Manoli, J. M.; Fraissard, J. *J. Chem. Soc., Chem. Commun.* **1992**, 464.
(69) Bastow, T. J. *Z. Naturforsch., A: Phys. Sci.* **1994**, *49*, 320.
(70) Willans, M. J.; Feindel, K. W.; Ooms, K. J.; Wasylishen, R. E. *Chem.—Eur. J.* **2005**, *12*, 159.
(71) Hamaed, H.; Lo, A. Y. H.; Lee, D. S.; Evans, W. J.; Schurko, R. W. *J. Am. Chem. Soc.* **2006**, *128*, 12638.
(72) Aurentz, D. J.; Vogt, F. G.; Mueller, K. T.; Benesi, A. J. *J. Magn. Reson.* **1999**, *138*, 320.
(73) Madhu, P. K.; Johannessen, O. G.; Pike, K. J.; Dupree, R.; Smith, M. E.; Levitt, M. H. *J. Magn. Reson.* **2003**, *163*, 310.

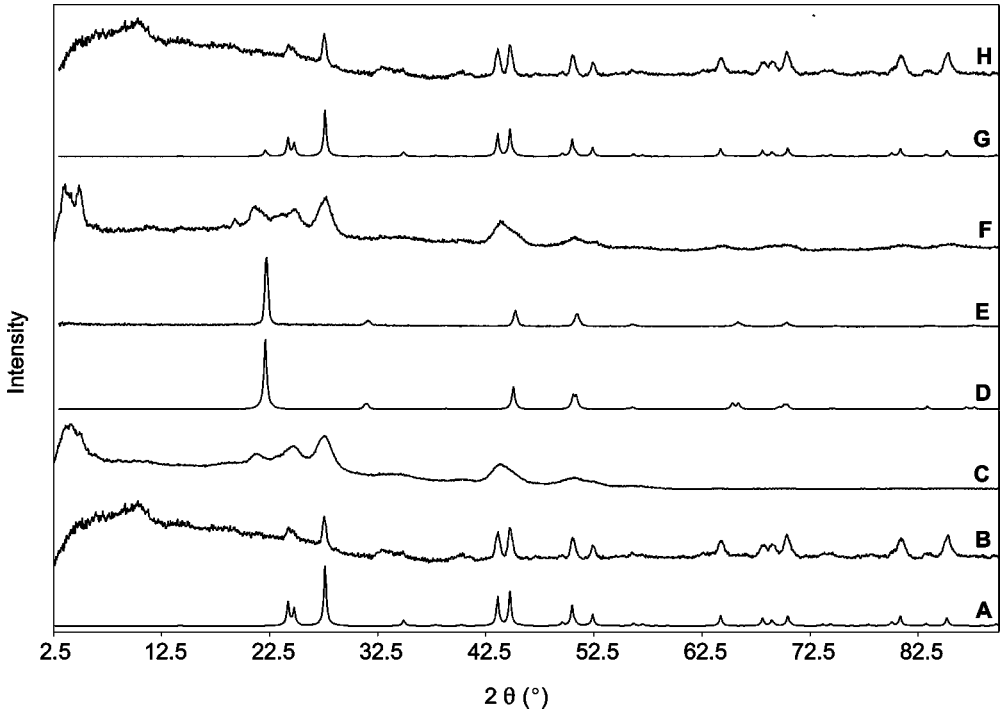

Figure 2. Powder X-ray diffraction patterns of (A) simulation and (B) experimental of **1**, (C) experimental of **2**, (D) simulation and (E) experimental of **9**, and (F) experimental of **7**. (G) and (H) are the calculated and experimental, respectively, powder XRD patterns composed of 90% of **1** and 10% of **9**.

Pure LaF_3 NPs, 2. Pure and Eu^{3+}-doped LaF_3 NPs have previously been characterized by powder XRD experiments,[23,74] which demonstrate that the cores are crystalline. In addition, the broadening of the diffraction peaks was used to estimate the size of the NPs, which range from 8 to 10 nm. Qin and co-workers utilized powder XRD, TEM, and electron diffraction experiments to probe the structure of Yb^{3+}/Er^{3+}-doped LaF_3 NPs. XRD data revealed that the NPs are highly crystalline with a hexagonal structure (unit cell dimensions of $a = 0.716$ nm and $c = 0.733$ nm, space group $P6_322$), and TEM images showed hexagonal morphology with an average edge length of ca. 15 nm.[75] The XRD pattern of pure LaF_3 NPs presented herein (Figure 2C) is consistent with previous data, confirming the presence of a crystalline LaF_3 phase with a distribution of environments resulting from the small NP size. The diffraction peak at $2\theta \approx 5°$ is indicative of some degree of NP organization or packing.

Solid-state ^{19}F and ^{139}La NMR spectra are shown in Figures 3−5. A comparison between the ^{19}F NMR spectra of **1** and **2** (Figure 3A,B) reveals that resonances with chemical shifts and integrated intensities corresponding to the F1 and F(2,3) fluorine sites are still observed for the NPs. There is significant broadening and a reduced signal-to-noise (*S*/*N*) ratio in the spectrum of **2**, such that the F2 and F3 resonances cannot be distinguished, and spinning sidebands are not observed. The chemical shift values corresponding to F1 and F(2,3) resonances are −23.1 and 22.0 ppm and have full widths at half-height (fwhh or $\Delta\nu_{1/2}$) of 9.8 and 11.0 kHz, respectively, compared to fwhh values of F1, F2, and F3 resonances of 2.9, 2.5, and 2.5 kHz, respectively, in the spectrum of **1**. The broadening of the NMR pattern is consistent with the small NP size and long-range disorder arising from differentiation of fluorine sites in the core and near the surface (i.e., size effects), as suggested by the powder XRD data. Broadening does not arise from $^{19}F-^{19}F$ dipolar couplings, since the applied spinning speeds far exceeded the magnitudes of such couplings ($^{19}F-^{19}F$ dipolar coupling constant is on the order of 5.5 kHz based on the shortest F−F distance in the crystal structure of **1**). In the spectrum of **2**, the broad, weak powder pattern observed in the low-frequency direction (ca. −200 to −650 ppm) arises from the background ^{19}F signal from the probe and sample spacers (Figure S3). This background signal is observed in all ^{19}F NMR spectra of NPs since *S*/*N* is limited by the low mol % of ^{19}F nuclei (due to the stabilizing ligands) and extremely long ^{19}F longitudinal relaxation time constants (reduced number of total acquisitions).

The ^{139}La MAS NMR spectra of **1** and **2** (Figure 4A,B) have the same centers of gravity and similar distributions of CT spinning sidebands, and no new resonances are observed, indicating that the La sites are similar in both the bulk material and NPs. The fine detail in the spectrum of **1** which arises from the second-order quadrupolar interaction, and the sharp spinning sidebands, are not observed in that of **2** due to inhomogeneous broadening, which is again consistent with long-range disorder and small NP size. A similar observation is made for the static Hahn-echo ^{139}La NMR spectra of **1** and **2** (Figure 5A,B). As in the case of the ^{19}F NMR data, there are not expected to be significant contributions to line broadening from $^{139}La-^{19}F$ dipolar couplings in either the MAS or static spectra, since they are completely averaged by fast MAS in the former and make negligible contributions to the broad powder pattern in the latter ($^{139}La-^{19}F$ dipolar coupling constants are calculated from known bond lengths to be on the order of 1 kHz).[55]

The combination of XRD and NMR data confirms that the local LaF_3 structure in the NPs is similar to that in the bulk phase. The ^{19}F and ^{139}La NMR powder patterns are inhomo-

(74) Tao, X.-j.; Zhou, J.-f.; Zhang, Z.-j.; Dang, H.-x. *Huaxue Yanjiu* **2000**, *11*, 8.
(75) De, G.; Qin, W.; Zhang, J.; Zhao, D.; Zhang, J. *Chem. Lett.* **2005**, *34*, 914.

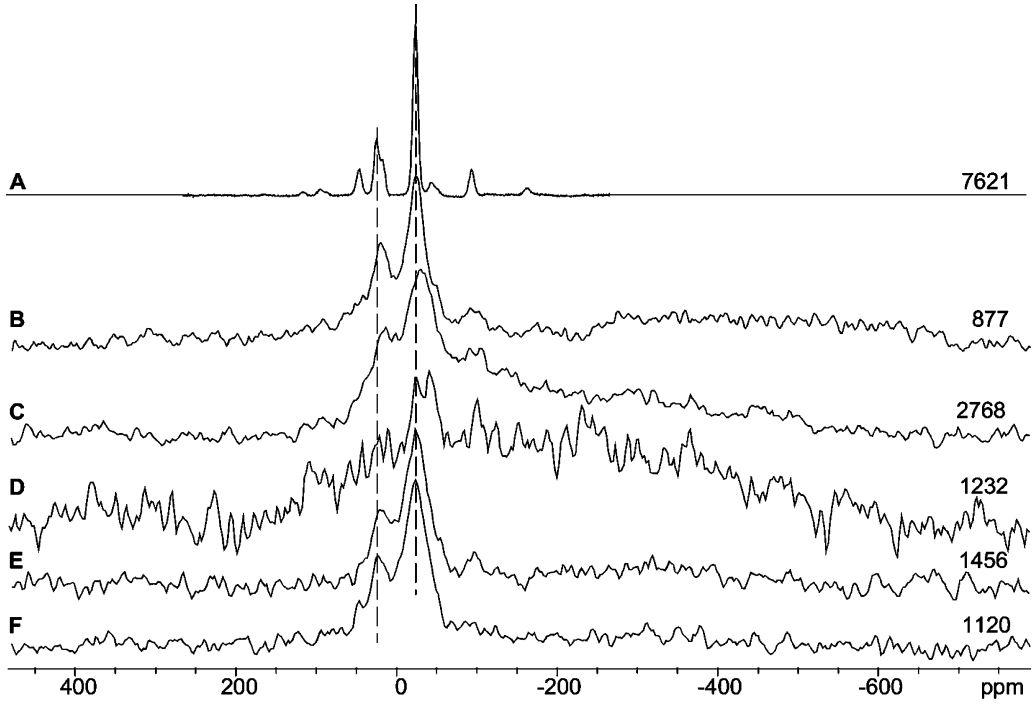

Figure 3. ^{19}F MAS NMR spectra of (A) **1**, (B) **2**, (C) **3**, (D) **4**, (E) **5**, and (F) **6** acquired at 9.4 T. Numbers of scans for each NMR spectrum are indicated on the right. Spinning frequencies of all NMR spectra range from 26 to 27 kHz. Dashed lines indicate the positions of F1 and F(2,3) sites in **1**.

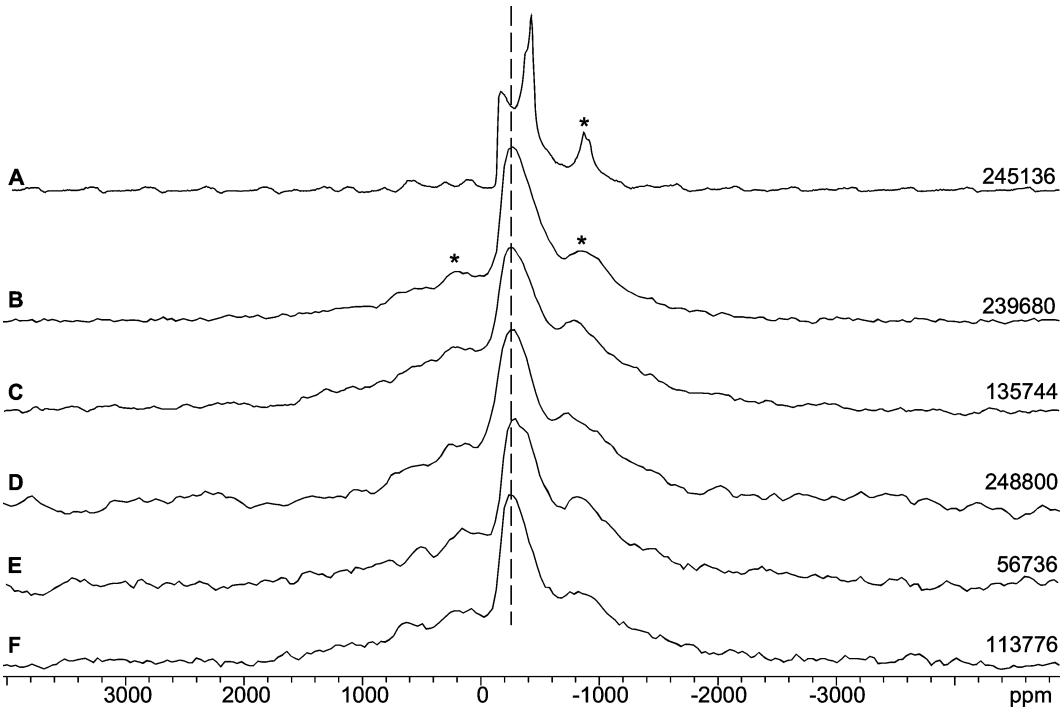

Figure 4. ^{139}La MAS NMR spectra of (A) **1**, (B) **2**, (C) **3**, (D) **4**, (E) **5**, and (F) **6** acquired at 9.4 T. The symbol "*" denotes a spinning sideband. Numbers of scans of each NMR spectrum are shown on the right. Spinning frequencies of all NMR spectra range from 28 to 30 kHz. The dashed line indicates that there is no paramagnetic shift in (C) and (D).

geneously broadened due to a distribution of ^{19}F and ^{139}La chemical shifts and ^{139}La quadrupolar interactions. This results from both the small sizes of the NPs and the presence of surface-bound ligands, since the ^{19}F and ^{139}La nuclei in the core of the NP exist within different electronic environments and, hence, experience different magnetic interactions than those near the NP surface. The net broadening is the result of a continuum of slightly different environments from the core to the surface. The NMR interactions in the NPs therefore largely resemble that of the pristine LaF_3, and unique, unusual resonances are not observed. Such broadening effects in NMR powder patterns of NPs are well-known.[76−80] For instance, Douglass et al. observed

(76) Thayer, A. M.; Steigerwald, M. L.; Duncan, T. M.; Douglass, D. C. *Phys. Rev. Lett.* **1988**, *60*, 2673.
(77) Tomaselli, M.; Yarger, J. L.; Bruchez, M., Jr.; Havlin, R. H.; deGraw, D.; Pines, A.; Alivisatos, A. P. *J. Chem. Phys.* **1999**, *110*, 8861.
(78) Ladizhansky, V.; Vega, S. *J. Phys. Chem. B* **2000**, *104*, 5237.
(79) Mikulec, F. V.; Kuno, M.; Bennati, M.; Hall, D. A.; Griffin, R. G.; Bawendi, M. G. *J. Am. Chem. Soc.* **2000**, *122*, 2532.

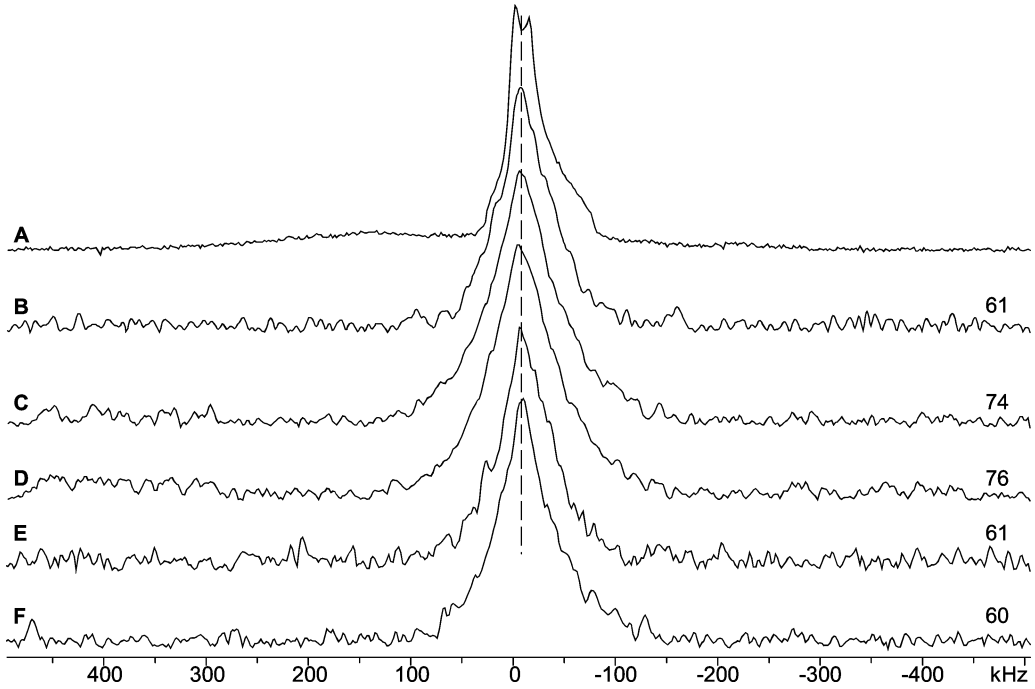

Figure 5. Static ^{139}La NMR spectra of (A) **1**, (B) **2**, (C) **3**, (D) **4**, (E) **5**, and (F) **6** acquired at 9.4 T. Numbers on the right indicate the fwhh (±2 kHz) of corresponding static spectra, and the dashed line marks the center of gravity of the pattern.

similar line broadening effects in solid-state ^{77}Se NMR experiments on a series of CdSe samples with different molecular sizes. A single, high *S*/*N* ^{77}Se peak is observed for the bulk CdSe, but line broadening and/or an increase of the number of ^{77}Se resonances is observed as the size of the NP decreases.[76]

LaF_3 NPs Doped with Paramagnetic Yb^{3+} Ions, 3 and 4. ^{171}Yb NMR experiments conducted on Yb^{3+}-doped NPs (5 and 10 mol % relative to La in Ln-doped LaF_3 NPs) do not yield observable signals, since Yb^{3+} is paramagnetic. However, ^{19}F and ^{139}La NMR experiments may provide insight into whether and how the paramagnetic ions are incorporated into the NP core. The ^{19}F MAS NMR spectra of **3** and **4** are shown in Figure 3C and D, respectively. In comparison to the spectra of **2**, the 5 mol % Yb^{3+} doping of **3** shifts the ^{19}F resonances to low frequency very slightly but broadens them significantly. The increased 10 mol % doping of **4** broadens the resonances further, such that the F1 resonance is barely detectable and the F(2,3) resonance disappears completely. The *S*/*N* in the spectrum of **4** is quite low due to the paramagnetic broadening and long ^{19}F T_1 constants (a recycle delay of 60 s was applied). The *S*/*N* of the F1 resonance is considerably reduced, and the center of gravity shifts to −34 ppm (compared to −23.1 ppm in the spectrum of **2**). The increased broadening of the powder patterns with higher sample doping arises predominantly from paramagnetic relaxation induced by unpaired electrons and possibly anisotropic broadening resulting from dipolar coupling with the unpaired spin density on the Yb atom.[81,82] The extreme broadening makes it impossible to accurately measure the isotropic chemical shift; however, the apparent negative shift may result from a pseudo-contact interaction with the unpaired electron.[49] The most important feature of the ^{19}F NMR spectra of **3** and **4** is the absence of intense, unshifted, and unbroadened resonances, indicating that the Yb^{3+} dopants are homogeneously distributed throughout the LaF_3 NP cores. This is consistent with both powder XRD data and luminescence decay measurements from Eu^{3+} emission spectra in previous works.[16,17,22]

The ^{139}La MAS NMR spectra of **3** and **4** (Figure 4C,D, respectively) are very similar to those of **2**, as are the corresponding static ^{139}La NMR spectra (Figure 5C,D). The centers of gravity of the MAS and static powder patterns are not influenced by a paramagnetic shift, likely because the paramagnetic dopants are not in the first coordination sphere of the La sites. However, the fwhh of the static ^{139}La NMR spectra increases from 61(2) to 76(2) kHz as the doping level increases from **2** to **4** (Figure 5B to 5D). Possible origins of this broadening include increased paramagnetic relaxation efficiency due to unpaired electrons (as in the case of the ^{19}F NMR spectra) and/or a wider distribution of chemical shifts and/or quadrupolar interactions due to local structural variations from doping.[83] To confirm the origin of this broadening, a series of ^{139}La relaxation measurements was conducted.

^{139}La Relaxation Measurements. ^{139}La T_1 and T_2 time constants were measured for **1**, **2**, and **4** at room temperature (Table 1). Unfortunately, due to the extremely long recycle delays and low *S*/*N* inherent in the ^{19}F NMR experiments, ^{19}F relaxation measurements are not reported for these systems. ^{139}La relaxation data for each sample were fitted using both mono- and biexponential functions. The latter involves two components which represent "fast" and "slow" mechanisms in the relaxation process and are denoted as T_{1f} (or T_{2f}) and T_{1s} (or T_{2s}). The existence of multiple relaxation mechanisms for NMR nuclei undergoing slow motions in a variety of solid materials is well-known.[84] The biexponential curve fits are in

(80) Berrettini, M. G.; Braun, G.; Hu, J. G.; Strouse, G. F. *J. Am. Chem. Soc.* **2004**, *126*, 7063.
(81) Mustafa, M. R.; Jones, W. E.; McGarvey, B. R.; Greenblatt, M.; Banks, E. *J. Chem. Phys.* **1975**, *62*, 2700.
(82) McGarvey, B. R. *J. Chem. Phys.* **1976**, *65*, 955.
(83) Matsushita, M.; Kato, T. *Chem. Phys. Lett.* **1997**, *273*, 291.
(84) Abragam, A. *Principles of Nuclear Magnetism*; Oxford University Press: Ely House, London W.1, 1961.

Table 1. ^{139}La T_1 and T_2 Relaxation Data Extracted from Mono- and Biexponential Functions for Bulk LaF_3 (**1**), Pure (**2**), and 10 mol % Yb^{3+}-Doped LaF_3 NPs (**4**)

	monoexponential[a]		biexponential					
	A	T_1 (ms)	X^2 [b] (%)	A_f	T_{1f} (ms)	A_s	T_{1s} (ms)	X^2 (%)
1	0.96(1)	146.39(560)	0.15	0.17(1)	13.44(303)	0.80(1)	234.71(1051)	0.03
2	0.72(3)	1.04(16)	1.15	0.36(5)	0.19(6)	0.44(5)	6.67(202)	0.61
4	0.89(2)	0.70(11)	1.05	0.28(7)	0.04(3)	0.61(7)	1.85(58)	0.59

	monoexponential[a]		biexponential					
	B	T_2 (μs)	X^2 (%)	B_f	T_{2f} (μs)	B_s	T_{2s} (μs)	X^2 (%)
1	0.69(5)	490(50)	0.53	0.61(42)	20(10)	0.42(1)	890(30)	0.02
2	0.97(9)	70(10)	0.86	0.74(30)	20(3)	0.30(2)	330(30)	0.01
4	0.98(6)	40(6)	0.42	0.77(23)	20(2)	0.23(2)	190(20)	0.01

[a] Mono- and biexponential functions used in relaxation-curve fittings are defined in the Experimental Section. [b] X^2 values are calculated by an equation of the form $\langle x_{exptl} - x_{calcd}\rangle^2$, where x_{exptl} and x_{calcd} represent experimental and calculated data points.

better agreement with experimental data, as indicated by smaller X^2 values (best fits are found in the Supporting Information, Figures S4 and S5). The T_{1s} components are the dominant components for longitudinal relaxation (slightly to much higher weighting than T_{1f}). For transverse relaxation, the T_{2f} components are more heavily weighted but, interestingly, vary little between samples; however, the T_{2s} constants are quite disparate. Similar trends in relaxation behavior are predicted for samples **1**, **2**, and **4** in both mono- and biexponential curve fits; accordingly, reference is made to the former in the ensuing discussion for simplicity.

The longitudinal relaxation rates are significantly increased (i.e., values of T_1 time constants decrease) in the NPs compared to the bulk. The T_1 of **2** is approximately 2 orders of magnitude smaller than that of **1**; however, the T_1 in **4** is only slightly smaller than that in **2**. Similar behavior is observed for the transverse relaxation, where the T_2 decreases from 490 (**1**) to 70 (**2**) to 40 (**4**) μs. The large decrease of T_1 and T_2 in **2** and **4** compared to **1** may at first seem puzzling, since quadrupolar relaxation is expected to be the dominant mechanism in these samples and the ^{139}La quadrupolar interaction does not vary significantly between samples. The reduction in relaxation time constants in the NPs with respect to the bulk material could result from the presence of a dipolar relaxation mechanism (i.e., from the abundant mobile protons in the surface ligands)[85] or possibly the presence of some paramagnetic impurities introduced during synthesis.[86] The latter is unlikely, since there is a very modest decrease in T_1 and T_2 constants from **2** to **4** resulting from paramagnetic relaxation. Another possibility is that the relaxation time is greatly enhanced by some sort of quantum size effect, though such effects are only well understood and defined for metal NPs.[87] A temperature-dependent relaxation study of NPs of various sizes and modeling of these data is beyond the current scope of this paper.

The effective spin−spin relaxation time constant, T_2*, is related to the line width of the powder pattern: $(\pi\Delta\nu_{1/2})^{-1} = T_2$*. Though this relationship holds strictly for Lorentzian lineshapes, a rough approximation of T_2* for **2** and **4** can be estimated from their static ^{139}La NMR patterns. The fwhh values of **2** and **4** are 61 and 76 kHz, respectively (Figure 5B,D), corresponding to T_2* values of ca. 4.19 and 5.21 μs, which are much smaller than their corresponding T_2 time constants (40 and 70 μs, respectively). Obviously, the breadths and shapes of the patterns largely result from a distribution of second-order quadrupolar interactions; but interestingly, the inverse of the difference in powder pattern widths, 21.2 μs, approximately equals the difference in their T_2 constants (30 μs). Hence, the difference in broadening of the ^{139}La NMR patterns of **2** and **4** arises chiefly from T_2 relaxation and not from the presence of distinct La environments in these samples.

LaF_3 NPs Doped with Diamagnetic Y^{3+} Ions, 5 and 6, and Bulk Crystalline YF_3, 8. Neither the ^{19}F MAS nor the ^{139}La MAS and static NMR spectra of **5** and **6** (parts E and F in Figures 3, 4, and 5, respectively) are significantly different from those of **2**. The breadths of the static ^{139}La NMR powder patterns of **2**, **5**, and **6** are almost identical (ranging from 60(2) to 61(2) kHz, Figure 5). The similarity of the NMR spectra of the Y^{3+}-doped and pure LaF_3 NPs strongly indicates that there are no major structural changes upon doping and the local LaF_3 structure remains largely the same. This confirms similar conclusions drawn above from the NMR spectra of paramagnetic-doped NPs, where the spectra are substantially different in appearance from those of the pure NPs, but only because of the presence of unpaired electrons at the Yb^{3+} sites.

In order to explore the nature of the metal dopant environments, solid-state ^{89}Y NMR experiments were conducted upon the 10 mol % Y^{3+}-doped NPs (**6**) and bulk YF_3 (**8**). While it was possible to acquire high S/N ^{19}F−^{89}Y CP/MAS NMR spectra for **8** (Figure S6), signals corresponding to Y^{3+} sites in the NP were not observed; rather, two narrow ^{89}Y resonances were observed which may correspond to unreacted $Y(NO_3)_3 \cdot 6H_2O$ embedded in the LaF_3 matrix (δ_{iso}(^{89}Y) of $Y(NO_3)_3 \cdot 6H_2O$ = −53 ppm).[88] ^{89}Y is a 100% naturally abundant spin-$^1/_2$ nucleus and subject only to anisotropic chemical shielding and heteronuclear dipolar interactions; however it is extremely unreceptive due to its low gyromagnetic ratio, $\gamma(^{89}Y) = -1.3163 \times 10^7$ rad T^{-1} s^{-1}, which results in low S/N NMR signals, acoustic probe ringing which obliterates FIDs, and large longitudinal relaxation time constants. In addition to this, since the number of Y^{3+} sites are considerably dilute (i.e., Y^{3+} doping is 10 mol %), it is not surprising that broad ^{89}Y NP resonances corresponding to Y located in La sites in the LaF_3 matrix were not observed.

(85) Ladizhansky, V.; Hodes, G.; Vega, S. *J. Phys. Chem. B* **1998**, *102*, 8505.
(86) Shames, A. I.; Panich, A. M.; Kempinski, W.; Alexenskii, A. E.; Baidakova, M. V.; Dideikin, A. T.; Osipov, V. Y.; Siklitski, V. I.; Osawa, E.; Ozawa, M.; Vul, A. Y. *J. Phys. Chem. Solids* **2002**, *63*, 1993.
(87) van der Klink, J. J.; Brom, H. B. *Prog. Nucl. Magn. Reson. Spectrosc.* **2000**, *36*, 89.
(88) Wu, J. J.; Boyle, T. J.; Shreeve, J. L.; Ziller, J. W.; Evans, W. J. *Inorg. Chem.* **1993**, *32*, 1130.

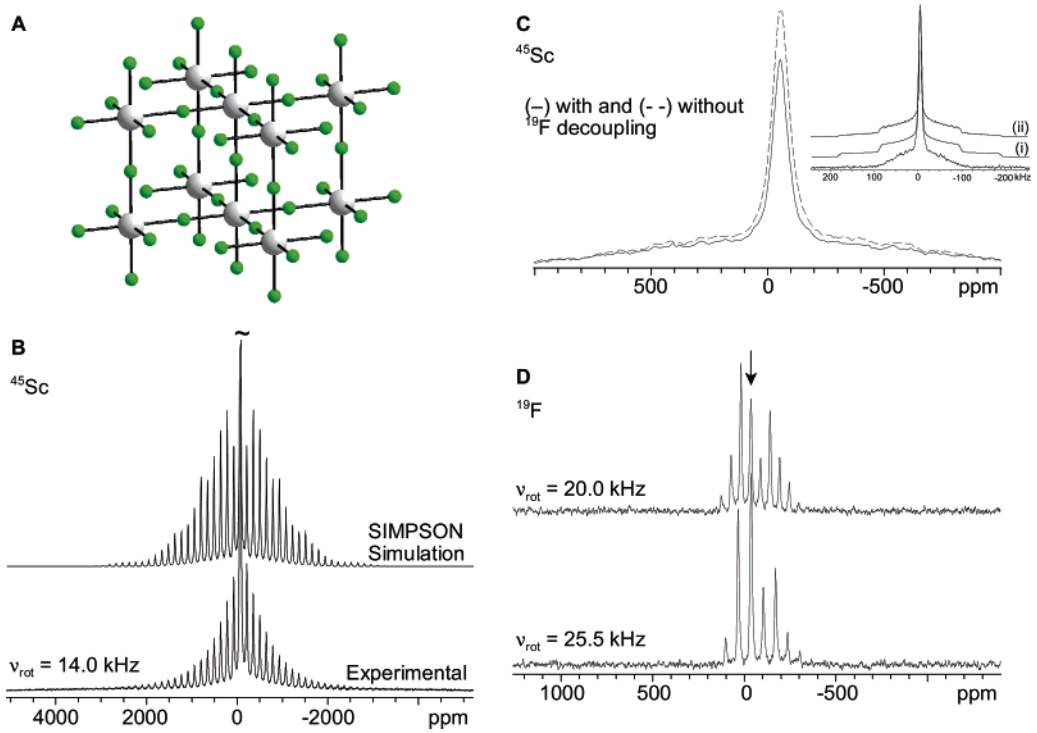

Figure 6. (A) Extended X-ray structure of ScF_3. (B) SATRAS and (C) static ^{45}Sc, and (D) ^{19}F MAS NMR spectra at 9.4 T of **9** (the arrow indicates isotropic ^{19}F resonance). Inset of (C): full spectrum of the ^{19}F-decoupled static ^{45}Sc powder pattern of ScF_3 along with the (i) analytical (perfect excitation) and (ii) numerical (imperfect excitation) simulation, showing partial excitation of the STs.

LaF_3 NPs Doped with 10 mol % Diamagnetic Sc^{3+} Ions, 7, and Bulk ScF_3, 9. Since ^{89}Y signals could not be observed, ^{45}Sc NMR experiments were conducted to examine the Sc environments in Sc^{3+}-doped NPs and bulk ScF_3. ^{45}Sc ($I = {}^7/_2$) is an extremely receptive NMR nucleus, being 100% naturally abundant and possessing a high magnetogyric ratio (6.5088×10^{27} rad T^{-1} s^{-1}). It has a moderately sized quadrupole moment ($Q(^{45}Sc) = -0.22 \times 10^{-28}$ m^2),[59] so the second-order quadrupolar lineshapes should not broaden and reduce the signal beyond detection limits, which is significant given the low doping level.

The X-ray structure of ScF_3 (**9**) predicts single Sc and F sites in the unit cell,[36−38] and the powder XRD pattern presented herein (Figure 2E) confirms the crystallinity and purity of the sample. The Sc atom is coordinated by six F atoms in an almost perfectly octahedral arrangement, which bond to neighboring Sc atoms to comprise an extended ScF_6 three-dimensional lattice (Figure 6A). While it is not expected that the Sc^{3+} sites in the NPs will be octahedral, the ^{45}Sc NMR of the bulk ScF_3 provides spectroscopic data for a reasonably comparable Sc environment (no other similar data are currently available in the literature). The ^{45}Sc{^{19}F} SATRAS and static ^{45}Sc NMR spectra of ScF_3 are displayed in Figure 6B and C, respectively. There is a small degree of long-range disorder in the sample, as indicated by the sloping spinning sideband manifolds; nevertheless, the scandium chemical shift is precisely measured at $\delta_{iso} = -52$ ppm, and the $C_Q(^{45}Sc)$ is estimated to be ca. 1.3(2) MHz. The small value of $C_Q(^{45}Sc)$ is consistent with the high spherical symmetry around ^{45}Sc. The partially excited inner satellite transitions can be seen flanking the central transition in the static spectrum (Figure 6C). Interestingly, comparison of ^{45}Sc and ^{45}Sc{^{19}F} NMR spectra reveal that the effects of ^{45}Sc−^{19}F dipolar coupling are very small, with the former spectrum only ca. 1 kHz wider than the latter. Given the proximity of the ^{45}Sc nucleus to the surrounding ^{19}F nuclei, and their large gyromagnetic ratios, this is somewhat surprising (Sc−F bond distance = 2.011 Å, giving rise to a ^{45}Sc−^{19}F dipolar coupling constant of ca. 3.4 kHz); however, it is possible that the dynamic motion of the fluorine atoms may partially average the dipolar interactions.[89] The ^{19}F MAS spectra of **9** (Figure 6D) reveal an isotropic chemical shift of −35.9 ppm, in good agreement with previously reported results.[90] The spinning sideband manifold arises largely from fluorine CSA, with a span of ca. 305 ppm and skew of 0.53 from Herzfeld−Berger analysis.[91]

The powder XRD and NMR data seem to indicate that the Sc^{3+} atoms are uniformly doped into La^{3+} positions and that pure ScF_3 is not observed. The powder XRD pattern of **7** (Figure 2F) resembles that of **2** (Figure 2C), except some higher angle peaks are observed which match positions in the mixed bulk LaF_3 and ScF_3 (Figure 2G,H). Once again, the broadened peaks are indicative of NP structure, and the low-angle peaks indicate some NP organization or packing. The ^{45}Sc MAS NMR spectra of **7** acquired at 9.4 and 21.1 T (Figure 7A,B) have an fwhh of ca. 11 kHz, significantly broader than that of **9** (fwhh of 3.4 kHz). The broadening prevents the accurate measurement of C_Q and δ_{iso} directly from the NMR spectra. The broadened powder patterns and absence of sharp spinning sideband manifolds are suggestive of both local disorder of the Sc sites (i.e., distribution of quadrupolar coupling constants and chemical shifts) and a significantly increased C_Q in comparison to that of the bulk material (which indicates the Sc^{3+} ions are not in octahedral environments). The centers of gravity of the NMR

(89) Du, L. S.; Schurko, R. W.; Lim, K. H.; Grey, C. P. *J. Phys. Chem. A* **2001**, *105*, 760.
(90) Avkhutskii, L. M.; Gagarinskii, Y. V.; Polishchuk, S. A.; Gabuda, S. P. *Spectrosc. Lett.* **1969**, *2*, 75.
(91) Herzfeld, J.; Berger, A. E. *J. Chem. Phys.* **1980**, *73*, 6021.

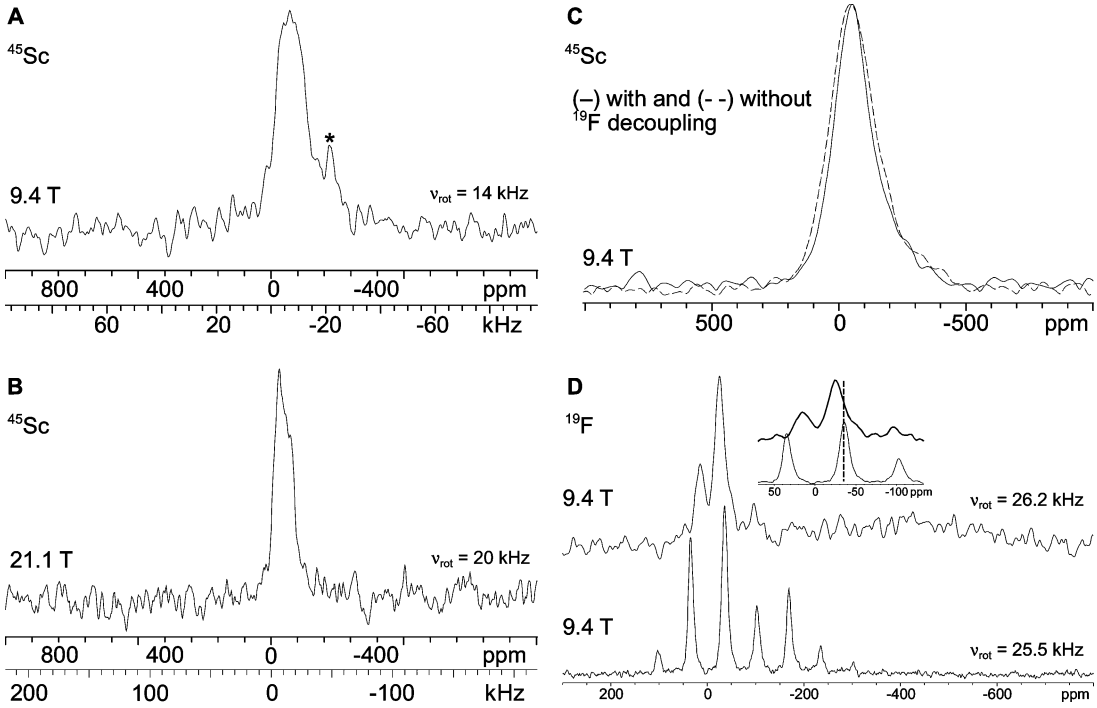

Figure 7. (A and B) ^{45}Sc MAS NMR spectra of **7** at multiple fields. (C) Static ^{45}Sc NMR spectra of **7**. (D) ^{19}F MAS NMR spectra of **7** (top) and **9** (bottom). Isotropic peaks in **7** and **9** are not at the same frequency. The symbol "*" denotes a spinning sideband in (A).

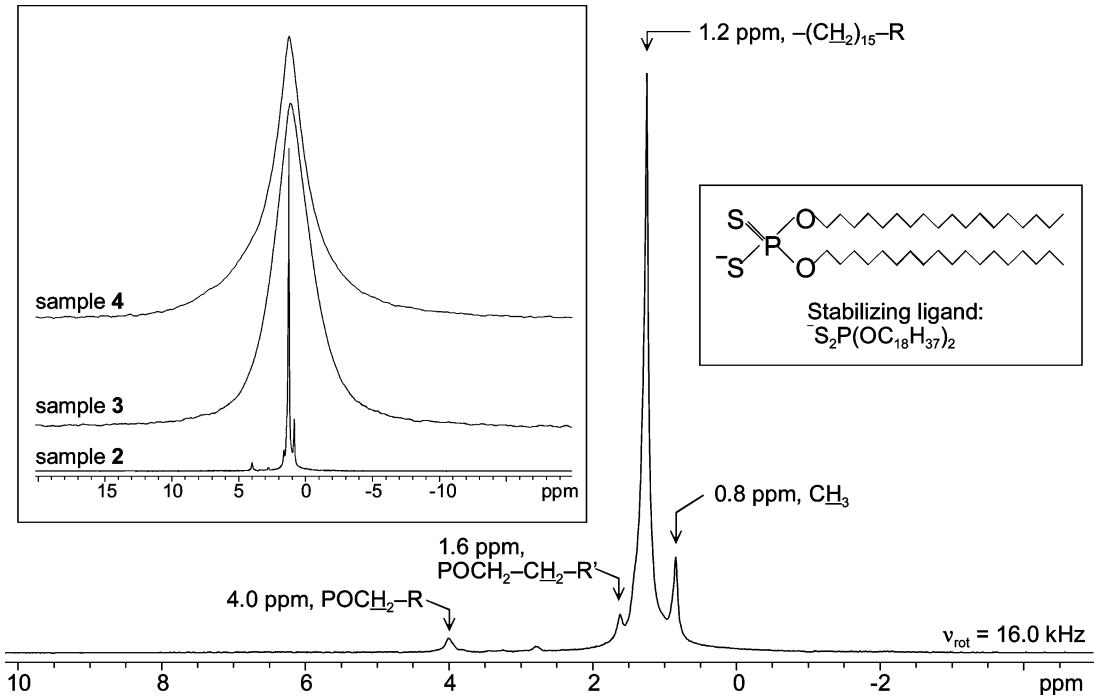

Figure 8. ^{1}H MAS NMR spectrum of **2** at 9.4 T. Inset on the left: a comparison among ^{1}H MAS NMR spectra of **2**, **3**, and **4** acquired at 9.4 T. Inset on the right: a schematic picture of the di-*n*-octadectyldithiophosphate stabilizing ligand.

patterns at 9.4 and 21.1 T are at −75.8 ppm and −45 ppm, respectively. The differences in the centers of gravity result from the reduction of second-order quadrupolar induced shifts upon moving to higher field, indicating that there is a significantly larger C_Q for **7** than in the case of **9**. The δ_{iso}(^{45}Sc) and the quadrupolar product, $P_Q = C_Q(1 + \eta_Q^2/3)^{1/2}$,[92] can be calculated by measuring the centers of gravity of the ^{45}Sc powder patterns obtained at two different magnetic fields and then solving two equations in two unknowns.[93] A unique solution of $\delta_{iso} = -37(5)$ ppm and $P_Q(^{45}Sc) = 12$ MHz is calculated. The δ_{iso} is similar to that measured for **9** but clearly indicates a distinct chemical shift environment. The P_Q indicates a potential range of C_Q between 12 and 14 MHz (depending upon the magnitude of η_Q), clearly indicating that the Sc nuclei are in spherically

(92) Mueller, K. T.; Baltisberger, J. H.; Wooten, E. W.; Pines, A. *J. Phys. Chem.* **1992**, *96*, 7001.

(93) Freude, D. In *Encyclopedia of Analytical Chemistry*; Meyers, R. A., Ed.; John Wiley & Sons Ltd, 2000; pp 1−37.

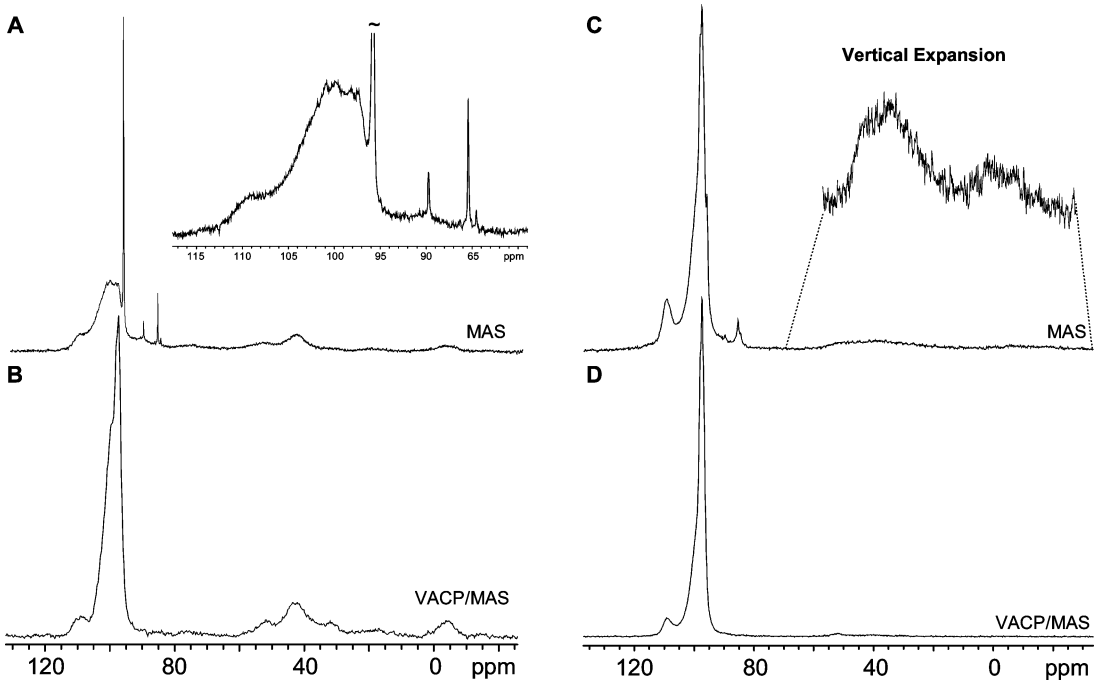

Figure 9. (A) $^{31}P\{^1H\}$ MAS and (B) $^1H-^{31}P$ VACP/MAS NMR spectra of **2**. (C) $^{31}P\{^1H\}$ MAS and (D) $^1H-^{31}P$ VACP/MAS NMR spectra of **4**. All NMR spectra were acquired at 9.4 T with a rotational frequency of 25 kHz. Insets: expansion of (A) showing sharp ^{31}P resonances, and vertical expansion of (C) about the thiophosphate and phosphate regions.

asymmetric environments. In addition, there is no unreacted $Sc(NO_3)_3$ present in these NPs, as this would yield an intense signal near $\delta_{iso} = -18.5$ ppm with a moderate $C_Q(^{45}Sc)$ around 6.2 MHz.[27] As in the case of the bulk sample, ^{19}F decoupling has little effect on the static ^{45}Sc NMR spectrum of **7** (Figure 7C). Further, the ^{19}F MAS NMR spectrum of **7** (Figure 7D) is similar to those of **2**, **5**, and **6**, the only difference being a slightly reduced *S*/*N* ratio in the spectrum of **7** (Figure S7). This and the absence of an isotropic peak corresponding to ScF_3 (Figure 7D, inset) support the retention of the local LaF_3 structure upon doping and that Sc^{3+} ions are occupying La positions in the LaF_3 core (i.e., the Sc atoms are not in octahedral environments).

Structure of the Inorganic NP Core - Summary. The combination of powder XRD and solid-state NMR data on bulk and NP samples allows for a number of conclusions to be made regarding the structure of the NP core. First, the inorganic core is crystalline, and the local structures of the La and F atoms are similar to that of the bulk material. Due to the small sizes of the NPs and presence of surface ligands, the local environments gradually change from the center to the surface of the NP giving rise to broad XRD peaks. This is confirmed by the inhomogeneously broadened NMR powder patterns arising from distributions of NMR interactions. Second, it is clear from both ^{19}F and ^{139}La NMR experiments that the low doping levels of early transition metal or lanthanide ions do not give rise to significant changes in the local structure of LaF_3 or the long-range structure in the NPs. Third, doping with paramagnetic Yb^{3+} ions leads to severe broadening of ^{19}F powder patterns and only moderate broadening of ^{139}La powder patterns, while no significant paramagnetically induced shifts are observed. This indicates that the paramagnetic ions are uniformly distributed throughout the NP and are located in the La positions in the extended LaF_3 structure (i.e., Yb^{3+} ions are more proximate to ^{19}F nuclei than ^{139}La nuclei). Finally, the ^{45}Sc NMR data show the complete incorporation of the Sc^{3+} ions into the extended LaF_3 structure and confirm that dopant ions occupy La^{3+} sites. This is direct evidence for positions of dopant lanthanide ions proposed in earlier papers.[16]

Chart 3. Functional Groups of Stabilizing Ligands: (A) Dithiophosphate, (B) Thiophosphate, and (C) Phosphate Heads, with R = $C_{18}H_{37}$; (D) Proposed Hydrolysis Process of the Dithiophosphate Groups in the Stabilizing Ligands

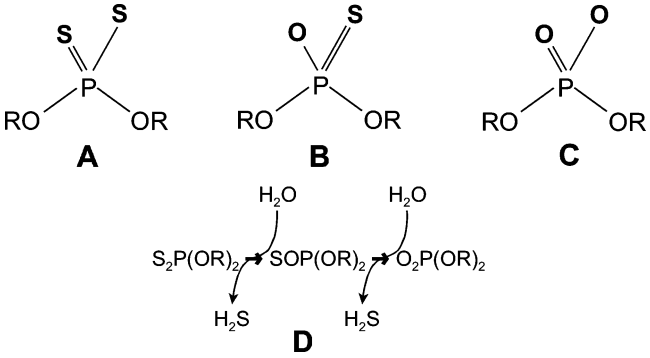

Characterization of Stabilizing Ligands by ^1H and ^{31}P NMR Spectroscopy. Solid-state ^1H and ^{31}P NMR experiments were applied to probe the nature of the stabilizing ligands (i.e., the di-*n*-octadectyldithiophosphate anion ($-S_2P(OC_{18}H_{37})_2$, Chart 1) on the surface of the NPs. Solid-state ^1H MAS NMR spectra of **2**, **3**, and **4** are shown in Figure 8. For **2**, a spinning speed of 16.0 kHz is enough to average the $^1H-^1H$ dipolar interactions almost completely, producing a solution-like spectrum. Peaks at 4.0 and 1.6 ppm are assigned to ethylene protons that are the closest and the next closest to the dithiophosphate group, respectively. The peak at 0.8 ppm is assigned to the terminal methyl protons, while the intense, broadened ^1H resonance at 1.2 ppm corresponds to the remaining ethylene protons. All peak assignments are in excellent agreement with solution NMR data.[17,22] In the ^1H MAS NMR spectra of **3** and **4** (inset of Figure 8), the fine structure of NMR spectrum

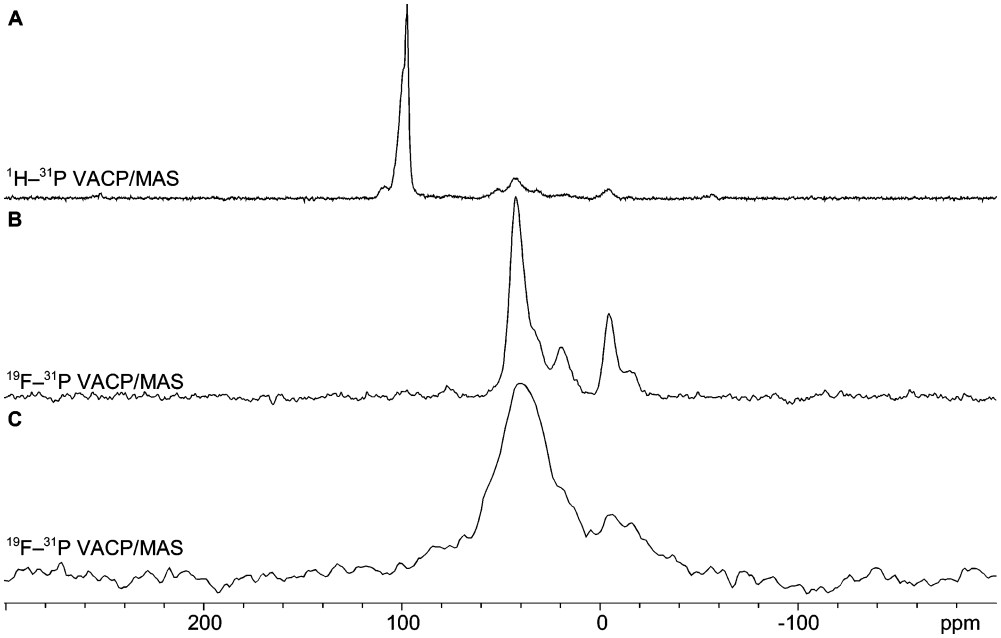

Figure 10. (A) ^{1}H−^{31}P MAS and (B) ^{19}F−^{31}P VACP/MAS NMR spectra of **2**. (C) ^{19}F−^{31}P VACP/MAS NMR spectra of **4**. All NMR spectra were acquired at 9.4 T with a rotational frequency of 25 kHz.

disappears completely, despite the higher spinning speeds. The powder pattern of **4** is considerably broader than that of **3**, undoubtedly due to the increased paramagnetic doping in the former. This is direct evidence for attachment of the ligands to the NP surface, since ^{1}H NMR signals of nuclei in the side chain are being broadened by unpaired electrons localized within the inorganic core of the NP.

^{31}P MAS and ^{1}H−^{31}P VACP/MAS NMR spectra of **2** (Figure 9A,B) are somewhat similar, with the exception of four sharp ^{31}P peaks positioned at 84.5, 85.4, 89.7, and 95.8 ppm in the former. There are three main ^{31}P resonances with centers of gravity at ca. 100, 40, and −4 ppm, which are inhomogeneously broadened from the distribution of distinct environments on the NP surface. The resonance centered at 100 ppm is assigned as a dithiophosphate resonance ($(RO)_2P(S)S$),[94] while the peaks at 40 ppm and −4 ppm correspond to thiophosphate ($(RO)_2P(S)O$[95−97] and phosphate ($(RO)_2P(O)O$) functional groups, respectively (Chart 3A to C).[96,98,99] The presence of thiophosphate and phosphate species is unexpected, though they may be formed by hydrolysis reactions during NP formation (Chart 3D).[100] The ^{31}P chemical shifts of the remaining four sharp minor peaks (Figure 9A, inset) fall into a range corresponding to a variety of forms of neutral[101] and anionic[102] phosphorus sulfides, such as P_4S_7 (81.9 to 112.8 ppm), α-P_4S_3 (84.5 and 91.0 ppm), PS_4^{3-} (88.5 and 103.3 ppm), $P_2S_7^{4-}$ (90.0 to 111.8 ppm), and $P_2S_6^{4-}$ (91.3 to 109.4 ppm). A ^{31}P MAS NMR experiment conducted on **4** after 3 months in a sample vial reveals almost no change in the thiophosphate and phosphate resonances; however, the intensity of the dithiophosphate powder pattern decreases, while an unassigned peak centered at ca. 86 ppm increases dramatically (Figure S8). Interestingly, phosphorus chemical shifts which correspond to the starting material in the synthesis of stabilizing ligand are absent (i.e., P_2S_5 and P_4S_{10}[16,17,22] have shifts of 49.7 and 51.6 ppm, respectively).[101]

^{31}P MAS and ^{1}H−^{31}P VACP/MAS NMR spectra of **4** (Figure 9C,D) appear to have only the resonance corresponding to the dithiophosphate species; however, vertical expansion of the thiophosphate and phosphate regions reveals broadened resonances (similar spectra are observed for **3**). It is possible that the two latter peaks are broadened due to relaxation by unpaired electrons at the Yb^{3+} ions in the NP cores or that partial hydrolysis has not occurred in this NP, thereby reducing the intensity of these peaks. To investigate this further, ^{19}F−^{31}P VACP/MAS NMR experiments were conducted on **2** and **4** (Figure 10). In the ^{19}F−^{31}P spectra of the pure and doped NP, large signal enhancements are obtained for the thiophosphate and phosphate resonances, while the dithiophosphate resonance is essentially absent. This could be due to the ^{31}P nucleus in the dithiophosphate group being further from the NP surface than ^{31}P nuclei in the thiophosphate and phosphate species (the signal for the phosphate species has the highest ^{19}F CP enhancement). Since the ^{19}F spin polarization originates from the NP, this is consistent with the paramagnetic relaxation of the ^{31}P resonances: the ^{31}P nuclei of the dithiophosphate species are distant enough from the NP surface that CP is very inefficient; conversely, the ^{31}P nuclei in the thiophosphate and phosphate species are proximate enough that CP efficiency is high.

Structure of the NP Surface - Summary. At the NP surface, di-*n*-octadectyldithiophosphate ligands are identified by both ^{1}H and ^{31}P NMR experiments. Broadening of the ^{1}H and ^{31}P NMR resonances in the Yb^{3+}-doped samples suggests that stabilizing

(94) McCleverty, J. A.; Kowalski, R. S. Z.; Bailey, N. A.; Mulvaney, R.; Ocleirigh, D. A. *J. Chem. Soc., Dalton Trans.* **1983**, 627.
(95) Bruzik, K.; Stec, W. J. *J. Org. Chem.* **1981**, *46*, 1625.
(96) Kudelska, W.; Michalska, M. *Tetrahedron* **1981**, *37*, 2989.
(97) Chojnowski, J.; Cypryk, M.; Fortuniak, W.; Michalski, J. *Synthesis* **1977**, 683.
(98) Satterthwait, A. C.; Westheimer, F. H. *J. Am. Chem. Soc.* **1980**, *102*, 4464.
(99) Jacob, L.; Julia, M.; Pfeiffer, B.; Rolando, C. *Synthesis* **1983**, 451.
(100) Corbridge, D. E. C. In *Studies in Inorganic Chemistry, Vol.2: Phosphorus: An Outline of its Chemistry, Biochemistry and Technology*, 2nd ed.; Elsevier Scientific Publishing Company: New York, 1980; Vol. 2, p 357.
(101) Eckert, H.; Liang, C. S.; Stucky, G. D. *J. Phys. Chem.* **1989**, *93*, 452.
(102) Schmedt auf der Gunne, J.; Eckert, H. *Chem.—Eur. J.* **1998**, *4*, 1762.

ligands are indeed coordinated to the NP surface. In addition, ^{31}P NMR data also identify a coexistence of dithiophosphate, thiophosphate, and phosphate species in the samples, though the dithiophosphate is predominant. The thiophosphate and phosphate species may be generated by hydrolysis reactions. ^{19}F−^{31}P VACP/MAS experiments reveal that the distances between the NP surface and the aforementioned functional groups vary, in the order of dithiophosphate > thiophosphate > phosphate, which suggests that La^{3+} surface sites interact with the O-containing head groups more strongly.

Conclusions

Multinuclear solid-state NMR data, in combination with powder X-ray diffraction measurements, have been used to gain insight into the local atomic and molecular structure in LaF_3 NPs. ^{19}F and ^{139}La NMR experiments give insight into the molecular structure of the core and effects of paramagnetic doping and, in combination with ^{45}Sc NMR experiments, into the dopant ion environments. The LaF_3 core of the NPs is relatively unperturbed compared to the bulk, but inhomogeneously broadened powder patterns indicate distributions of La and F sites from the core of the NP to its surface. Comparison of powder pattern shapes and relaxation time constants adds new insights into the differences between the structures of NPs and bulk parent materials. ^{1}H and ^{31}P NMR experiments identify an interesting surface chemistry, and the combination of paramagnetically doped samples and ^{19}F−^{31}P VACP/MAS experiments reveals the interface between the LaF_3 core and the dithiophosphate surface ligands. We anticipate that this study will encourage future solid-state NMR investigations on this important class of NPs.

Acknowledgment. The Natural Sciences and Engineering Research Council (NSERC, Canada), the Canadian Foundation for Innovation (CFI), the Ontario Innovation Trust (OIT), and the British Columbia Knowledge Development Fund (BCKDF) are gratefully acknowledged for financial support. R.W.S. and A.Y.H.L. also acknowledge the Centre for Catalysis and Materials Research (CCMR) at the University of Windsor, Ontario Graduate Scholarship (OGS) program, and Imperial Oil and NSERC CRD for additional funding.

Supporting Information Available: Tables of solid-state NMR experimental parameters, ^{139}La relaxation curve fits utilizing mono- and biexponential functions, and additional ^{139}La, ^{89}Y, ^{19}F, and ^{31}P NMR spectra. This material is available free of charge via the Internet at http://pubs.acs.org.

JA068604B